Designing self-organized nanopatterns on Si by ion irradiation and metal co-deposition

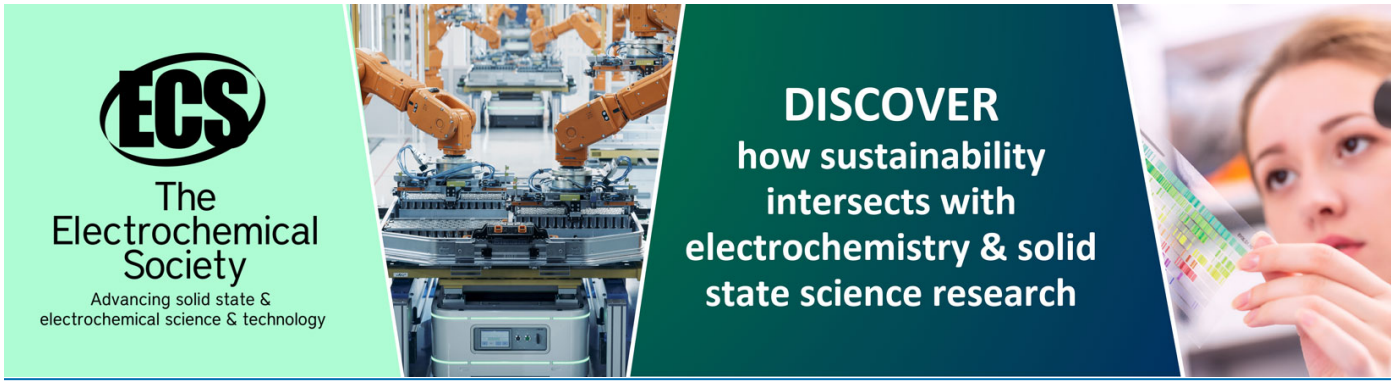

OPEN ACCESS
IOP Publishing
Nanotechnology

Nanotechnology **25** (2014) 085301 (11pp)
doi:10.1088/0957-4484/25/8/085301

Designing self-organized nanopatterns on Si by ion irradiation and metal co-deposition

K Zhang, O Bobes and H Hofsäss

II Physikalisches Institut, Universität Göttingen, Friedrich-Hund-Platz 1, D-37077 Göttingen, Germany

E-mail: hans.hofsaess@phys.uni-goettingen.de

Received 14 August 2013, revised 29 October 2013
Accepted for publication 20 November 2013
Published 4 February 2014

Abstract

Dot and ripple nanopatterns on Si surfaces with defined symmetry and characteristic dot spacings of 50–70 nm were created by 1 keV Ar ion irradiation at normal incidence and simultaneous co-deposition of Fe atoms at grazing incidence. Fe was continuously supplied from different sputter targets surrounding the Si substrate, leading to a steady-state Fe content in the near-surface region of the substrates. The pattern formation is self-organized, most probably caused by ion-induced phase separation. Patterns were analyzed with atomic force microscopy and the Fe content in the irradiated layer was measured with Rutherford backscattering. The symmetries of the produced patterns are isotropic, four-fold symmetric, three-fold symmetric and various types of two-fold symmetric patterns, depending on the geometrical arrangement of the sputter targets. Pattern formation was studied for a steady-state coverage of Fe between 0.5 and 3.3×10^{15} Fe cm^{-2}. The threshold coverage for the onset of pattern formation is about $0.5–1 \times 10^{15}$ Fe cm^{-2}. The coherence length of the patterns is comparable to the average dot spacing. Nevertheless, the autocorrelation analysis reveals a residual long-range periodicity of some patterns. The dot spacing can be adjusted between about 20 nm and several hundred nm depending on the ion species and ion energy.

Keywords: silicon, ion erosion, self-organized, pattern symmetry, dots and ripples

(Some figures may appear in colour only in the online journal)

1. Introduction

Nanostructured surfaces with tunable structure symmetry and tunable characteristic length scale and periodicity are of growing interest, e.g. for photonic applications [1], surface enhanced Raman spectroscopy [2, 3] and nanostructured biocompatible surfaces [4, 5]. The self-organized formation of ripple and dot nanostructures induced by low-energy ion irradiation is a simple, fast and maskless process to generate large-area nanopatterned surfaces. Ion-induced nanostructured metallic surfaces, such as arrays of metal nanowires, were investigated with regard to plasmonic functionality [6–8]. Ion-induced surface ripples on ferromagnetic thin films were found to create a tunable pronounced magnetic texture [9–14]. So-called wave-ordered nanostructures generated by low-energy nitrogen ion irradiation of Si were investigated as periodic nanomasks to dope the channel region of field-effect transistors [15].

Low-energy ion beam irradiation of surfaces under simultaneous co-deposition of small amounts of metal atoms gives rise to pronounced self-organized surface nanopatterns. In particular, Mo and Fe atoms, co-deposited on Si substrates simultaneously during ion irradiation at room temperature, induce pronounced dot and ripple patterns, even during normal and near-normal ion irradiation [16–21]. Without co-deposition the Si surface remains flat under near-normal ion irradiation [19, 20]. The formation of dot patterns at room temperature

by Mo seeding of an irradiated Si surface was first shown by Ozaydin *et al* for Mo co-deposition on ion-irradiated Si [16]. The influence of substrate temperature on pattern formation during Mo seeding was investigated by grazing-incidence small-angle x-ray scattering [17]. From a decreasing pattern height with increasing temperature up to 450 °C, it was concluded that (surface) diffusion of Mo to form protecting clusters is unimportant. Macko *et al* and Cornejo *et al* have confirmed that the frequently observed formation of dot and ripple patterns on Si at near-normal ion incidence could be attributed to the unintentional Fe co-deposition from sputtering of vacuum chamber walls [21, 22]. Dot and ripple patterns on Si are also formed by co-deposition of Ni, Pt and W, but not in the case of co-deposited Cu and Au atoms [23, 24]. The height of the patterns reaches several nm and the lateral length scale is on the order of 100 nm for 5 keV Xe ion irradiation. Surface patterns different from the well known ripple patterns are also formed on amorphous carbon during co-deposition of W and Ti [25].

In our recent work, we emphasized the important role of a steady-state surface coverage of metal atoms responsible for sputter yield attenuation and pattern formation and introduced the term surfactant sputtering [26]. In a subsequent publication we studied, in particular, the pattern formation on Si during Fe co-deposition and introduced a scenario to describe the pattern formation [20]. This scenario proposes ion-induced phase separation towards a metal silicide phase embedded in a Si matrix as the relevant mechanism. Indeed, the formation of amorphous Fe silicides was experimentally verified by XPS measurements [27]. Ion enhanced phase separation was also recently proposed to explain pattern formation on Si for oblique 40-keV Ar ion erosion and Fe co-deposition [28], and for 2 keV Kr irradiation of Si and simultaneous Fe co-deposition at 660 K [29]. To demonstrate the role of phase separation processes, we carried out experiments with different co-deposited metal atom species. In the case of systems which form disilicide (e.g. $FeSi_2$, $MoSi_2$) or mono-silicide (e.g. PtSi) phases, pronounced dot and ripple patterns are created and ion-induced phase separation is seen as the driving mechanism for pattern formation [23, 27]. In contrast, co-deposition during ion irradiation of Au or Cu, elements which either do not form silicides at all or only very metal-rich silicide phases, the surface remains flat. In particular the comparison of Cu versus Fe and Ni co-deposition as well as Au versus Pt and W co-deposition clearly demonstrates the important role of the chemical effects of the pattern formation, because the collision cascade effects of the two groups of elements are quite comparable. Phase separation is also supported by the observation that the surface remains flat when the Fe concentration in the Fe–Si surface layer reaches the $FeSi_2$ stoichiometry [27].

At the initial stage of ion irradiation and co-deposition, a flat amorphous metal–silicon surface layer with almost uniform composition forms as the steady state [20, 30]. Due to the ion-induced phase separation, local nanoscale regions with increased metal concentration are created [20, 31]. According to the scenario, slight variations in the sputtering yield are induced in this way, leading to the growth of nanoscale dot patterns with higher metal content in the dot regions. Since co-deposition of metal atoms occurs at grazing incidence, selective deposition and shadowing occurs and dots will start to propagate, possibly merging into ripples, depending on the steady-state metal coverage [32]. This dynamic behavior was recently also predicted theoretically [33]. For increasing steady-state metal coverage and fixed ion fluence, the surface topography evolves from a flat surface over dot patterns to ripple patterns [20, 21]. In the case of Fe, the surface remains flat if the coverage is below about 1.5×10^{15} Fe cm^{-2}, and a coverage higher than about 6.0×10^{15} Fe cm^{-2} is needed to form ripple patterns. The surface topography also evolves from dot patterns to ripple patterns for a fixed metal surface coverage and increasing ion fluence.

It was also shown that the orientation of ripple patterns induced by Fe co-deposition correlates with the direction of incidence of co-deposited atoms [19, 20]. The wavevector of ripples points opposite to the projected direction of the incident co-deposited atoms. This directional dependence motivated us to study the pattern formation using multiple sputter targets from co-deposition and demonstrate the design of dot or ripple patterns with predefined symmetry.

In this work we present experimental studies of the pattern formation on Si, induced by using Fe surfactant atoms. We use an Ar ion beam at normal incidence and co-deposition of Fe at oblique incidence angles using multiple Fe sputter targets positioned at different azimuthal angles around the Si substrate. We show that dot and ripple patterns with tailored isotropic, two-fold, three-fold, and four-fold symmetry can be created.

2. Experimental details

Single-crystalline Si(100) substrates of size 15×15 mm^2 with initial root mean square roughness of at most 0.1 nm were used. Prior to ion irradiation with 1 keV Ar ions at normal ion incidence, the Si samples were cleaned sequentially in an ultrasonic bath with acetone and methanol. The Si substrates were kept at room temperature during ion irradiation. Fe co-deposition was done with different sputter targets, positioned adjacent to the Si substrate. As target material we used ARMCO Pure Iron sheets (Fe—99.9%; C—0.01%; Mn—0.06%; P—0.005%; S—0.003%; Si-trace). The sheets were inclined with respect to the Si substrate normal by 30° or 70°.

We used different arrangements and geometries for the sputter targets, as shown in figure 1. The setup used is similar to our previous co-deposition experiments [20, 23, 26] and consists of inclined Fe sheets adjacent to the Si substrate. An isotropic Fe co-deposition from all azimuthal directions is obtained with a cylinder- or funnel-like sputter target (figure 1(a)). The target was positioned in front of the Si sample at distances of 0.8–2.5 mm between the Si surface and the bottom side of the cylinder. Different deposition rates were achieved by adjusting this target–substrate distance. The ion beam was incident perpendicular to the sample plane and also to the cylinder plane. Near the bottom of the cylinder, the inner side was inclined so that the beam irradiated the inner

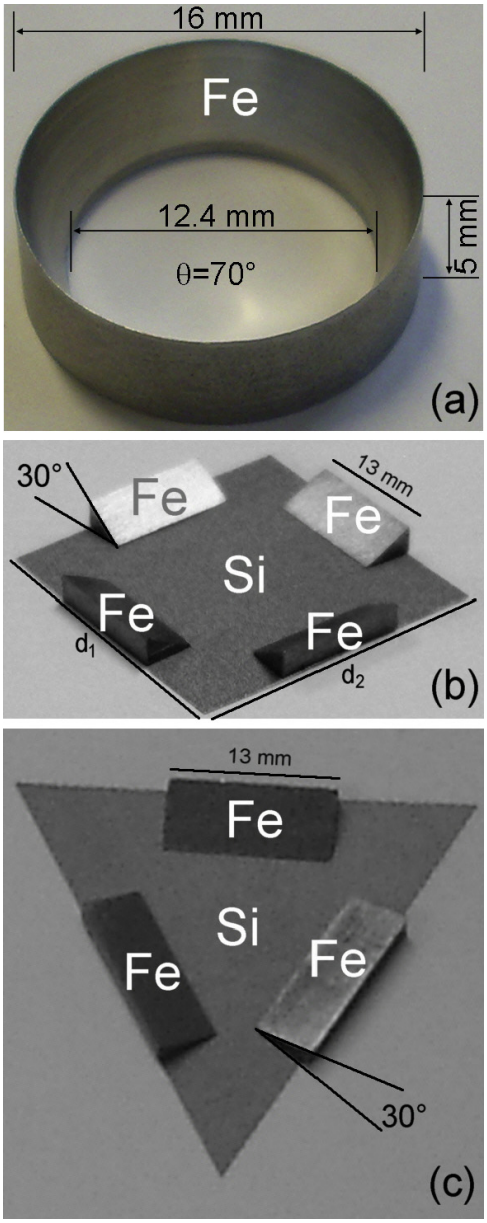

Figure 1. Images of the sputter target geometries: (a) cylindrical target with inner walls inclined at 70°, (b) four sputter targets positioned at 90° with respect to each other at the outer edges of a square Si substrate with spacings d_1 and d_2 of opposite targets, (c) three sputter targets positioned at 120° with respect to each other at the edges of an equilateral triangular Si substrate.

cylinder wall at a 70° ion incidence angle. Fe co-deposition from four azimuthal directions with an average angle of 90° between each direction was achieved with the setup shown in figure 1(b). The four Fe rods, with 13 mm width and an inclination angle of 30° with respect to the surface normal, were mounted on a square Si base plate. The Si sample for ion irradiation was then positioned in the center of the base plate. The amount of Fe co-deposition at the center position between these targets was adjusted by varying the spacings d_1 and d_2 between opposite targets. A similar setup with three-fold symmetry using three sputter targets is shown in figure 1(c). Because of the finite size of the sputter targets, the co-deposition direction has a certain azimuthal distribution, with the average co-deposition direction defined by the center position of the sputter target. Symmetric irradiation and co-deposition conditions are only fulfilled in the center region of the Si substrate. Therefore we analyzed, in particular, the patterns generated in this center region. We also analyzed patterns at several off-center spots of the samples.

The Si substrate and the Fe sputter targets were irradiated with 1 keV Ar ions from a Gen-II plasma ion source with an ion current of 150 μA cm^{-2}. Each sample was irradiated with a fluence of 2.5×10^{18} ions cm^{-2}. The ion beam is incident along the normal direction of the Si surface. The simultaneous irradiation of the sputter target and substrate with a single broad ion beam ensures a fixed ratio between the local co-deposition flux and the ion flux [23]. The metal coverage on different spots of the Si samples was quantitatively determined by Rutherford-backscattering spectroscopy (RBS) at the Göttingen 500 keV ion accelerator [34] with 900 keV He^{2+} ions and a beam spot of 1 mm diameter.

The surface topography of the sputter-eroded samples was analyzed by atomic force microscopy (AFM) in contact mode using a Nanosurf microscope and the Nanosurf Easyscan software. The Si cantilevers from NanoAndMore GmBH had a mean tip radius of 7 nm. For topography analysis, Fourier transformation statistical analysis and autocorrelation function analysis we used the open source software Gwyddion [35]. The discrete autocorrelation function (ACF) for a surface height profile $z(k, l)$ in an AFM image with $M \times N$ pixels of size $\Delta x \times \Delta y$ is given by

$$G(m,n) = \frac{1}{(N-n)(M-m)} \sum_{l=1}^{N-n} \sum_{k=1}^{M-m} z_{k+m,\,l+n}\, z_{k,l}, \qquad (2.1)$$

with $0 \le m < M, 0 \le n < N$, and distance between pixels $x_m = m \cdot \Delta x$ and $y_m = n \cdot \Delta y$. The coherence length of the noisy periodic pattern can be calculated from the envelope of $G(m, n)$ [36]. We extract the coherence length L from $G(m, n)$ normalized to

$$G(0,0) = \frac{1}{NM} \sum_{l=1}^{N} \sum_{k=1}^{M} z_{k,l}^2 = \overline{z^2}, \qquad (2.2)$$

by fitting a one-dimensional exponential envelope function

$$\frac{G_{\mathrm{env}}(m \cdot n)}{G(0,0)} = G_\infty + (1 - G_\infty) \cdot \exp(-r/L), \qquad (2.3)$$

along a given direction $r = (x \cos\theta, y \sin\theta)$. In our case the normalized ACFs approach a finite average value $G_\infty = \frac{\bar{z}^2}{\overline{z^2}}$ for large r, where $\bar{z} = \frac{1}{MN} \sum_{k=1}^{M} \sum_{l=1}^{N} z(k, l)$ is the average height in the AFM image with values $z(k, l) \ge 0$.

One dot pattern (shown in figure 11(b)) was grown using 10 keV Xe ions and co-deposition of Fe from a single target in order to demonstrate the variation of dot spacing with the ion irradiation conditions.

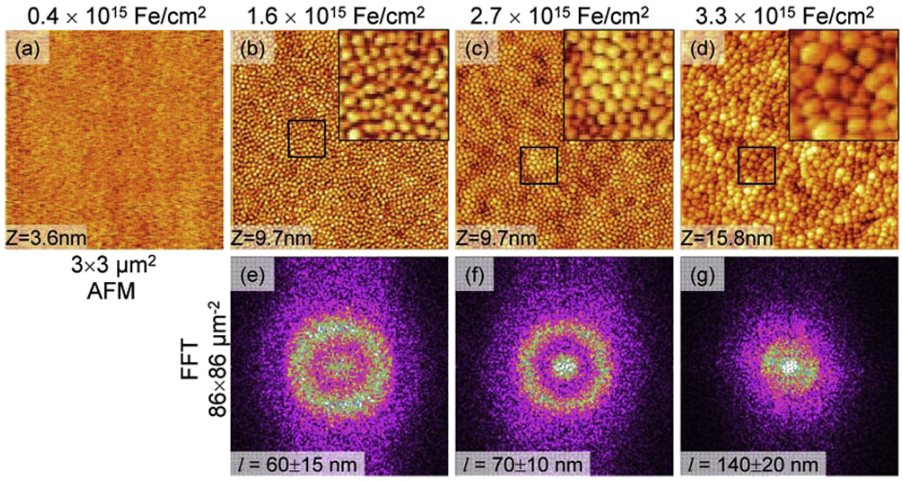

Figure 2. (a)–(d) AFM topography of a Si–Fe surface for increasing steady-state Fe coverage obtained by Ar ion irradiation and co-deposition of Fe using the cylindrical sputter target geometry shown in figure 1(a). *Z* is the range of the color height scale. The insets show the magnified 500 nm^2 regions marked by the squares. (e)–(g) Fast Fourier transformation (FFT) images of the AFM images (b)–(d) above. The characteristic dot spacing *l* related to the maximum in the FFT is also shown.

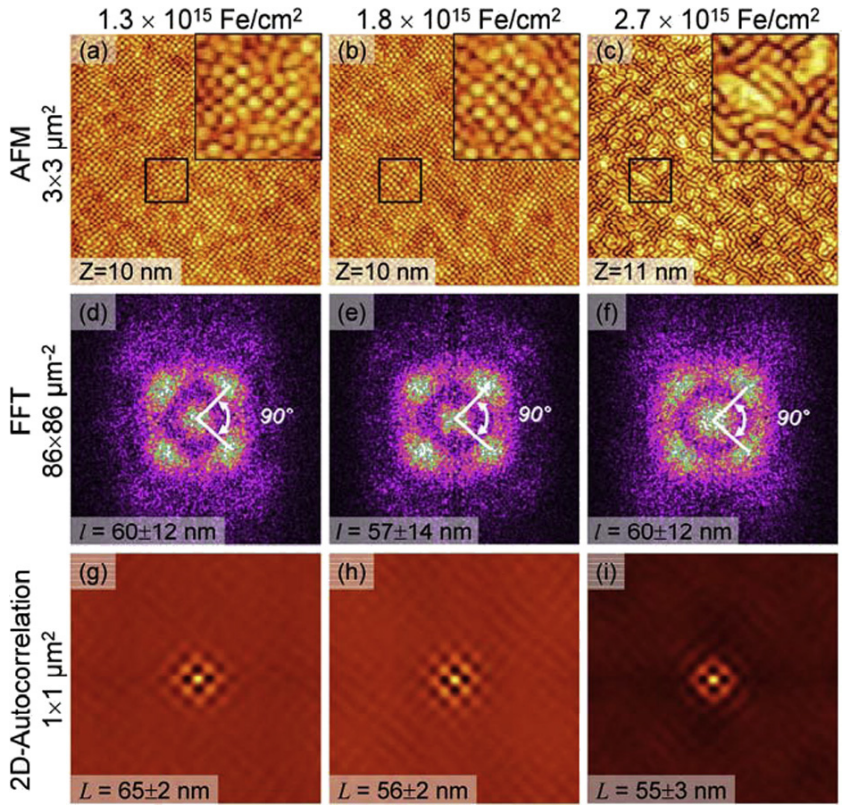

Figure 3. (a)–(c) AFM topography of a Si–Fe surface for increasing steady-state Fe coverage obtained by Ar irradiation and co-deposition of Fe using the four-fold symmetric sputter target geometry shown in figure 1(b). *Z* is the range of the color height scale. The inserts show the magnified 500 × 500 nm^2 regions marked by the squares. (d)–(f) Fast Fourier transformation (FFT) images of the AFM images (a)–(c) above. The dot spacing *l* related to the maxima in the FFT is also shown. (g)–(i) 2D-ACF of the AFM images (a)–(c). *L* is the coherence length as described in the text.

3. Results

Ion irradiation under isotropic azimuthal co-deposition of Fe using the cylindrical setup shown in figure 1(a) leads to an isotropic dot pattern when the steady-state Fe coverage exceeds about 1.0–1.5 × 10^{15} Fe cm^{-2} (figure 2). For lower Fe coverage the surface remains flat (figure 2(a)). With increasing Fe coverage, the characteristic dot spacing increases from about 60 nm at 1.6 × 10^{15} Fe cm^{-2} to about 140 nm at 3.3 × 10^{15} Fe cm^{-2}. Fast Fourier transformation (FFT) of

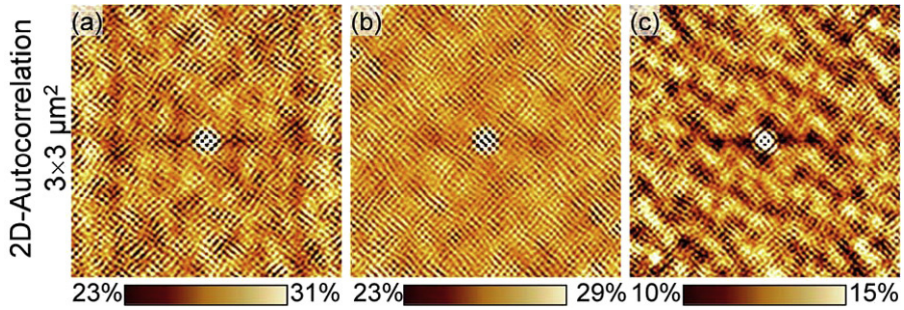

Figure 4. (a)–(c) Normalized 2D-ACF function of the AFM images shown in figures 3(a)–(c) with a compressed color scale compared to the 100% scale in the ACFs of figures 3(g)–(i).

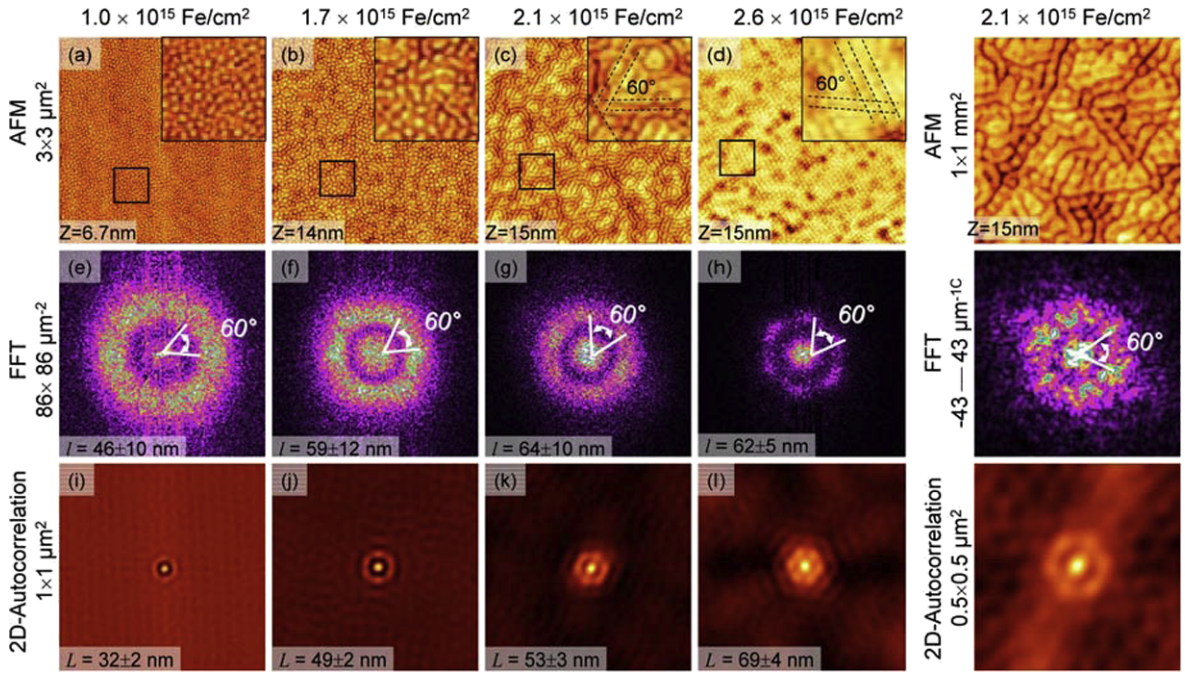

Figure 5. (a)–(d) AFM topography of a Si–Fe surface for increasing steady-state Fe coverage obtained by Ar irradiation and co-deposition of Fe using the three-fold symmetric sputter target geometry as shown in figure 1(c). *Z* is the range of the color height scale. The inserts show the magnified 500 × 500 nm^2 regions marked by the squares. (e)–(h) Fast Fourier transformation (FFT) images of the AFM images (a)–(d) above. (i)–(l) 2D-ACF of the AFM images (a)–(d).

the AFM images reveals an isotropic dot pattern. Only for the highest Fe coverage (figures 2(c) and (f)) does a slight indication of a texture appear.

Dot patterns with four-fold symmetry are shown in figure 3. The patterns were generated using the setup of figure 1(b) with four Fe sputter targets positioned symmetrically at 90° with respect to each other. The Fe coverage in the center region between the sputter targets was varied by adjusting the distance $d_1 = d_2$ between opposite Fe targets. The FFT images, and also the autocorrelation functions, clearly show the four-fold symmetry of the dot patterns with a characteristic dot spacing of about 60 nm. The pattern with the highest Fe coverage of 2.7×10^{15} Fe cm^{-2} has an additional structure with a larger characteristic length of about 200–400 nm and several spiral-like pattern segments. The longer length scale is related to the length of ripple ridges, which are probably formed by joining of adjacent dots (inset of figure 3(c)). The coherence length extracted from the envelopes of the ACFs is 55–65 nm and reflects the distribution of dot spacings. The 2D-ACFs shown in figure 4 are plotted with a compressed color scale to accentuate the outer regions. It is evident that the periodic pattern dephases within the coherence length. However, it is partially restored with a beat period of several hundred nm in one or the other direction. The amplitude of the ACF pattern is slightly modulated with the beat period. Due to the four-fold symmetry this leads to an ACF resembling a weaved basket meshwork (figure 4(b)). This behavior of the autocorrelation function resembles the superposition of two harmonic waves with similar period (see figure 4.7 of [36]). However, a bimodal distribution of dot distances cannot be seen in the FFTs shown in figure 3.

Dot patterns with three-fold symmetry are shown in figure 5. The patterns were generated using the setup of figure 1(c) with three Fe sputter targets positioned at 120° with

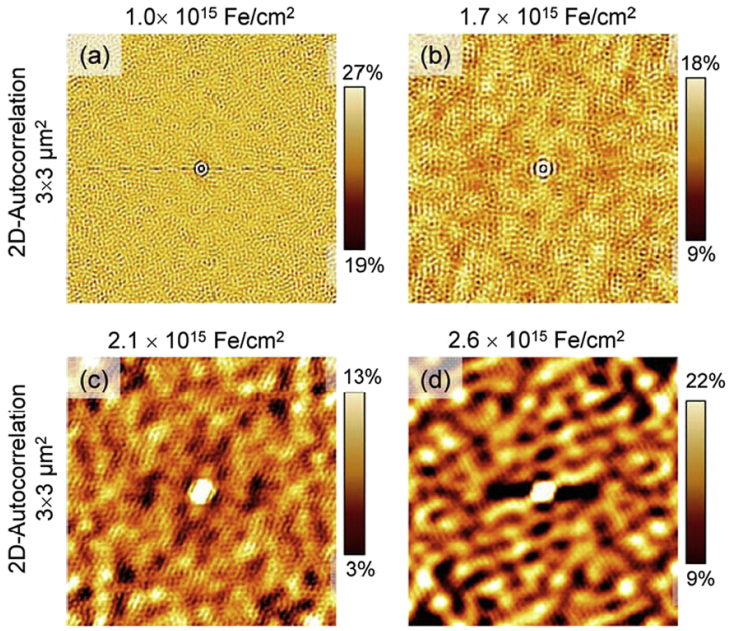

Figure 6. (a)–(d) Normalized 2D-ACF of the AFM images shown in figures 5(a)–(d) with a compressed color scale compared to the 100% scale in the ACFs of figures 5(i)–(l).

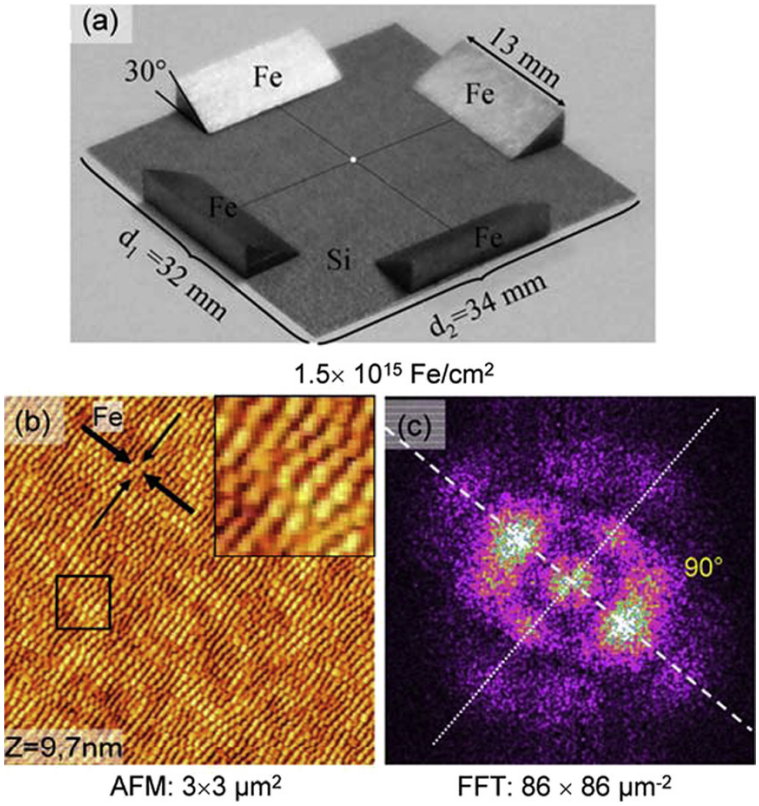

Figure 7. (a) Four-fold symmetric sputter target geometry as shown in figure 1(b) with different target spacings d_1 and d_2. The patterns were analyzed at the center position marked by a white dot. (b) AFM topography of a Si–Fe surface obtained by Ar irradiation and co-deposition of Fe using the sputter target geometry shown in (a). The arrows indicate the Fe co-deposition direction. The thickness of the arrows indicates the amount of Fe co-deposition. Z is the range of the color height scale. The inset shows a magnified 500 × 500 nm^2 region marked by the square. (c) Fast Fourier transformation (FFT) image of the AFM image (b) showing two superimposed ripple patterns with perpendicular wavevectors. The wavelength of the pronounced ripples is about $\lambda \approx 70$ nm, the wavelength of the weaker ripple pattern, leading to rows of dots along the ripple ridges, is $\lambda \approx 63$ nm.

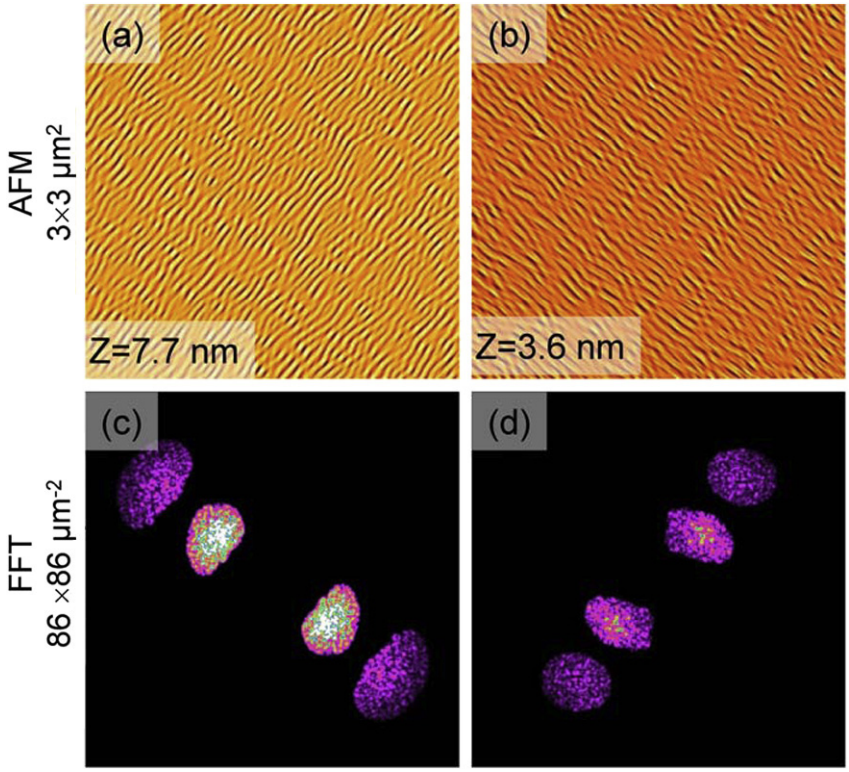

Figure 8. (a) and (b) Topography image of the Si–Fe surface as shown in figure 5 generated using only fractions of the FFT images as shown in (c) and (d). *Z* is the range of the color height scale. (c) and (d) Filtered fast Fourier transformation (FFT) images of the AFM image shown figure 7.

respect to each other. The Fe coverage in the center region between the sputter targets was varied by adjusting the distance between the Fe targets and the center position of the Si substrate. For the lowest Fe coverage of 1×10^{15} Fe cm^{-2} the FFT image and also the autocorrelation function indicate a rather isotropic dot pattern with small amplitude. With increasing Fe coverage, the three-fold symmetry of the patterns becomes more and more pronounced. The characteristic dot spacing increases from 45 ± 10 to 64 ± 10 nm. The patterns with Fe coverage higher than 2×10^{15} Fe cm^{-2} show an additional structure with a large characteristic length and several triangular pattern segments. In the insets in figures 5(c) and (d) rows of dots inclined by about 60° can be identified. The coherence length extracted from the envelope of the center region of the 2D-ACF increases from 32 nm to about 70 nm with increasing Fe coverage. The 2D-ACFs shown in figure 6 are plotted with a compressed color scale to accentuate the outer regions. The periodic pattern dephases within the coherence length. With increasing Fe coverage a coarse grained irregular structure appears.

AFM images taken at the center position but with different distances d_1 and d_2 of the surrounding Fe targets, as well as AFM images taken at off-center positions, reveal a variety of asymmetric dot or ripple patterns. An example of two superimposed ripple patterns with perpendicular wavevectors and wavelengths of about 70 nm is shown in figure 7. The pattern is obtained using the four-fold target geometry of figure 1(b), but with different distances d_1 and d_2 of opposite Fe targets. The amplitude of one pattern (corresponding to the FFT signals along the dashed line in figure 7) is significantly larger than the other pattern (corresponding to the FFT signals along the dotted line in figure 7), so that the height of the ripple ridges is modulated with a wavelength of about 60–70 nm. The superimposed ripple patterns can be seen more clearly in figures 8(a) and (b), where the topography images are generated using the filtered FFT images shown in figures 8(c) and (d).

Dot patterns obtained with the symmetric four-fold target geometry but measured at an off-center position exhibit a two-fold symmetry and are shown in figure 9. For these patterns, the FFT indicates two prominent orientations with comparable characteristic dot spacings of about 70 nm, which are not perpendicular but inclined at an average angle around 100° (figures 9(d) and (e)). Interestingly, magnified regions of the AFM images show different orientations of rows of dots. The orientation sometimes changes rather abrupt (insets 2 of figures 9(b) and (c)) or gradually (inset 1 of figure 9(b)). The gradual variation of the orientation of rows is related to a decreasing or increasing spacing of dots between neighboring rows. A certain orientation extends for typically 4–6 dots, in a few cases up to 10 dots. The dashed lines in the insets in figures 9(b) and (c) are almost parallel to the average projected co-deposition direction from the left and right sputter target. The dotted lines indicate the approximate projected co-deposition direction from the front and back sputter target. The inclination angle between rows, indicated as dashed lines in figures 9(b) and (c), is around 20°. The inclination angle between rows indicated as dashed lines and rows indicated

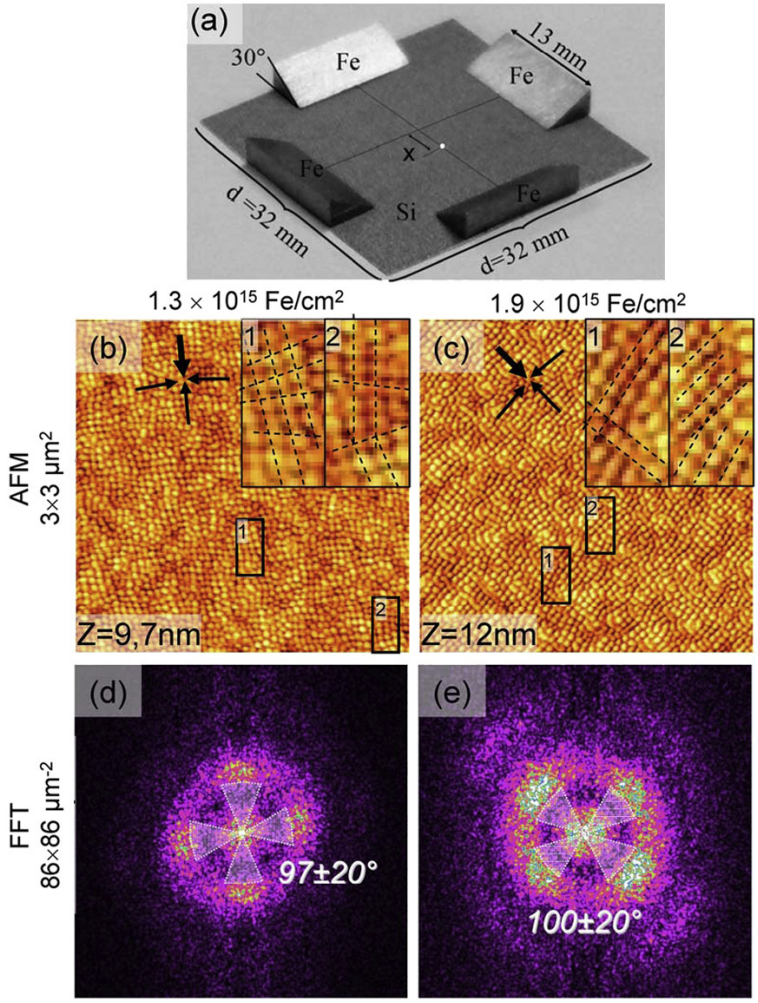

Figure 9. (a) Four-fold symmetric sputter target geometry as shown in figure 1(b). The patterns were analyzed at the off-center position marked by a white dot. (b) and (c) AFM topography of the Si–Fe surface obtained by Ar irradiation and co-deposition of Fe using the target geometry as shown in (a) taken at two different off-center positions with different Fe coverage. Z is the range of the color height scale. The insets show two magnified 250×500 nm^2 regions marked by the squares. (d) and (e) Fast Fourier transformation (FFT) image of the AFM images (b) and (c) showing a two-fold symmetry of the dot patterns. The average orientation of rows of dots is inclined around 100°. The dot spacing is $l \approx 70$ nm.

as dotted lines in figures 9(b) and (c) varies between about 85°–110°. The inclination between dashed and dotted lines in inset 1 of figure 9(c) is close to 100°. The alignment of the rows of dots and the angle of 100° ± 20° seen in the FFT is in accordance with the geometry of the off-center position with respect to the surrounding Fe targets. A characteristic angle of 10° is indicated in figure 9(a).

A dot pattern with superimposed almost perpendicular wavevectors, but with significantly different wavelengths of 55 and 200 nm, is shown in figure 10. The pattern is obtained by co-deposition of Fe mainly from two of the four sputter targets with a rather broad azimuthal distribution. Also the Fe content of 3.2×10^{15} Fe cm^{-2} in the analyzed off-center position is rather high, so that coalescence of dots into rather extended ripples occurs.

4. Discussion

We have presented several examples of dot and ripple patterns created by metal surfactant sputtering of Si using multiple sputter targets and ions incident normal to the Si substrate. The examples show that the known strong dependence of the pattern orientation on the direction of surfactant atom co-deposition [19, 20] can be utilized to tailor the symmetry and characteristic length scale of dot and ripple patterns. In particular, for normal ion incidence, the pattern symmetry is solely determined by the geometrical arrangement of the multiple metal sputter targets surrounding the substrate. In our irradiation setup the symmetric four-fold and three-fold patterns appear only at the central symmetry position of the substrate with four or three symmetrically arranged surrounding sputter targets. Patterns with different characteristic length scales along different directions, asymmetric patterns or superimposed patterns with different amplitudes and wavelengths are obtained either at off-center positions or by varying the distance between opposite sputter targets. In the case of off-center positions and the symmetric four-fold target geometry (figure 9), the dot patterns exhibit rather abrupt changes in the orientation of rows of dots. It seems that within

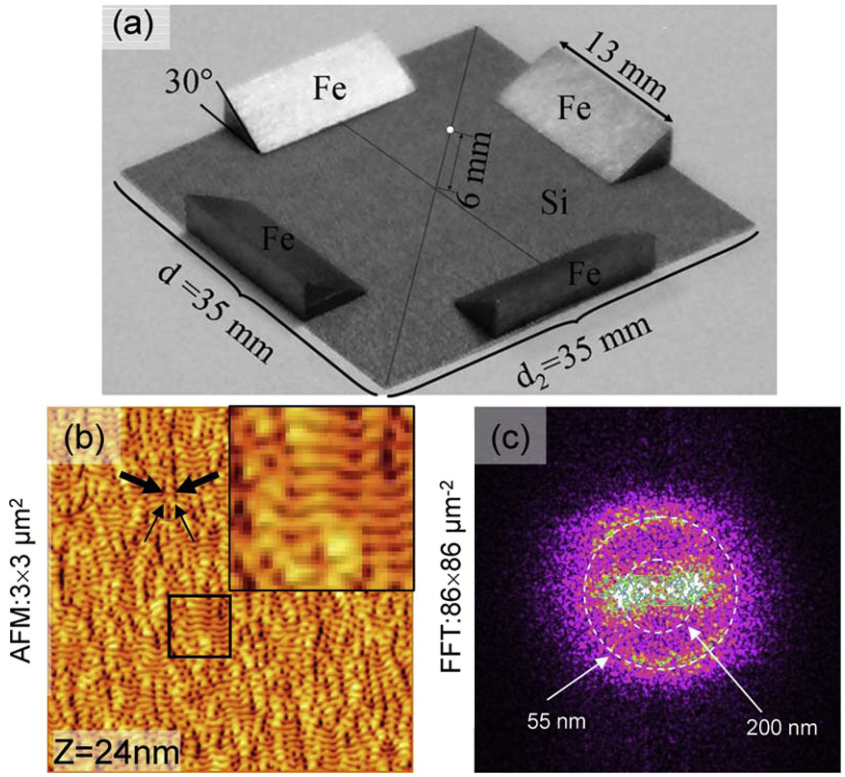

Figure 10. (a) Four-fold symmetric sputter target geometry as shown in figure 1(b). The patterns were analyzed at the off-center position marked by a white dot. (b) AFM topography of a Si–Fe surface measured at the off-center position. Z is the range of the color height scale. The insets show the magnified 500 nm^2 regions marked by the squares. (c) Fast Fourier transformation (FFT) image of the AFM image (b) shows a ripple pattern with about 55 nm wavelength and a superimposed perpendicular pattern with a wavelength of about 200 nm. This perpendicular pattern leads to a modulation of the height of the ripple ridges, as can be seen in the insets of (b).

a limited spatial region the orientation of rows of dots is determined by the geometric position of one of the surrounding Fe targets.

The physical process leading to dot patterns at low Fe coverage and ripple patterns at higher metal coverage is believed to be due to ion-induced phase separation [20, 23, 27]. The characteristic spacing of dots and the characteristic wavelength of ripple patterns is probably related to the processes leading to ion-induced phase separation. In the present study with 1 keV Ar ions and Fe surfactant atoms, the dot spacing is about 50–70 nm. A coarsening of the pattern and an increasing dot spacing occurs at higher Fe coverage, exceeding average Fe concentrations of about 10 at.% within the ion-irradiated surface region. An average dot spacing of 50 nm under comparable irradiation conditions was also observed by other groups [18, 19, 21, 37, 31]. A narrower dot spacing of 30 nm was found after 500 eV Ar irradiation of Si with Mo co-deposition [17]. In our previous studies with 5 keV Xe and various metal surfactant atoms we observed a dot spacing of 100–150 nm [23]. Ziberi *et al* found an increase of the ripple wavelength from 40 to 70 nm with increasing Ar ion energy from 500 eV to 2 keV for patterns on Si, which most probably were induced by Fe co-deposition [38]. A similar study, where ripple patterns were also probably induced by Fe co-deposition, showed a ripple wavelength decreasing from about 75 to 45 nm with ion incidence angle increasing from 0° to 30° and for 2 keV Xe ions [39]. At least for low ion energies the metal atoms will be distributed within the thickness of the irradiated layer, due to recoil collisions and ion-induced diffusion. The average dot spacing as a characteristic pattern length scale may therefore depend on the thickness of the irradiated layer. We estimate the layer thickness by $d \approx r_P + 2\sigma$ with the projected range r_p and straggling σ calculated with SRIM [40]. As error for d we assume the straggling σ. We obtain $d \approx 4.4$ nm for 500 eV Ar ions, $d \approx 6.5$ nm for 1 keV Ar ions, $d \approx 13$ nm for 5 keV Xe ions and $d \approx 19$ nm for 10 keV Xe ions. The relationship between the layer thickness and the characteristic dot spacing is plotted in figure 11(a). The AFM image of size 6×6 μm^2 plotted in figure 11(b) shows an isotropic dot pattern, which we obtained by 10 keV Xe irradiation of Si at normal ion incidence and Fe co-deposition at oblique incidence. The dot spacing determined from the power spectral density is $l = 162 \pm 26$ nm. The approximately linear increase of the dot spacing with layer thickness shown in figure 11(a) indeed shows that the characteristic pattern length scale can be tuned between about 20 nm and several hundred nm by proper selection of the ion energy and ion species. The linear relation may not be valid at higher ion energies, because the co-deposited metal atoms will then be confined in a near-surface region rather than through the whole thickness of the ion-irradiated layer determined by the ion range.

The coherence length of the pattern with a dominant symmetry was extracted from the envelope of the autocorrelation

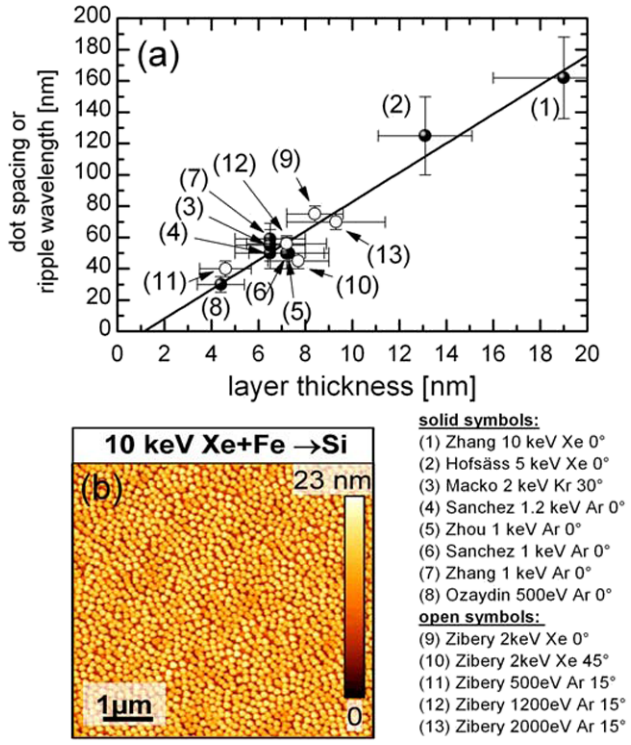

Figure 11. (a) Measured characteristic dot spacing or ripple wavelength as a function of the thickness of the irradiated layer for patterns formed on Si by normal or near-normal ion incidence and co-deposition of Fe or Mo. The solid line is a linear fit to the data points. References to data with solid symbols: (1) this work (b), (2) [23], (3) [19, 21], (4) [18], (5) [31], (6) [37], (7) this work, (8) [17]. References to data with open symbols: (9)–(13) [38, 39]. (b) AFM image of a dot pattern with 160 ± 26 nm dot spacing, generated with 10 keV Xe irradiation of Si at normal incidence and Fe co-deposition.

functions. In all cases, a coherence length comparable to the dot spacing was found, which means that the periodicity of a row of dots is preserved for only a few dots before a phase jump or a defect in the pattern structure occurs. Typically, rows with up to ten equally spaced dots can be identified in the AFM images. However, different rows are usually aligned along the symmetry axes of the patterns.

In previous studies a threshold of the steady-state metal coverage for surfactant or impurity-induced pattern formation was found [19, 20, 27]. In the case of Fe on Si and 5 keV Xe this threshold is about 1.5×10^{15} Fe cm^{-2}. The threshold found in the present study using 1 keV Ar is around $0.5–1 \times 10^{15}$ Fe cm^{-2}. The experiment-specific threshold metal coverage σ_{Th}, which is usually determined by RBS, may be converted to a more universal threshold concentration within the ion-irradiated surface layer of thickness d, given by $c_{\mathrm{Th}} \approx \sigma_{\mathrm{Th}} \cdot d$. The required threshold atomic concentration of Fe to induce pattern formation on Si is then about $c_{\mathrm{Th}} \approx$ 2.5 at.%.

5. Conclusions

Self-organized formation of dot and ripple nanopatterns on Si surfaces with predefined symmetry of the patterns and an adjustable dot spacing can be achieved by keV ion beam irradiation with ions incident in the direction normal to the surface and simultaneous oblique incidence co-deposition of metal atoms from multiple sources. The symmetry of the patterns can be tuned from isotropic, four-fold symmetric, three-fold symmetric and various types of two-fold symmetric patterns, depending on the geometrical arrangement of the metal sputter targets surrounding the substrate. In general, the geometrical arrangement of sputter targets determines the local metal atom/ion arrival ratio and the directional dependence of metal co-deposition. Larger area dot patterns with defined symmetry may be obtained by using more distant sputter targets, which then require separate ion sources for each sputter target. In this contribution, we have demonstrated pattern formation with a designed symmetry for Fe co-deposition on Si. However, other disilicide-forming metal atoms co-deposited on Si at oblique incidence during ion irradiation and supplied from different sputter targets surrounding the Si substrate should also give rise to similar dot and ripple patterns. The method can therefore be applied to other co-deposited metals, preferably elements such as Ni, Mo and W forming stable metal disilicides. Dot patterns with predefined symmetry may also be obtained for amorphous carbon (a-C) surfaces and various carbide-forming co-deposited metal atoms.

In accordance with previous observations we find a threshold steady-state metal coverage for the onset of pattern formation. For 1 keV Ar ions and Fe co-deposition this threshold corresponds to about 2.5 at.% Fe within the irradiated surface layer. The dot pattern formation process is most likely caused by ion-induced phase separation. For 1 keV Ar ion irradiation and Fe co-deposition we obtain patterns with characteristic dot spacings or wavelengths of 50–70 nm. For 10 keV Xe the dot spacing increases to about 160 nm. We propose that the dot spacing is related to the ion range or the mean depth of the irradiated layer, and can be adjusted by selecting the ion energy and ion species.

The patterned silicide or carbide surfaces presented here may be coated with thin films to obtain specific desired surface properties. These self-organized nanostructured surfaces with designed symmetry and length scale may be of interest, e.g. for photonic applications [1], surface enhanced Raman spectroscopy [2, 3] or nanostructured biocompatible surfaces [4, 5].

Acknowledgment

This work was funded by the Deutsche Forschungsgemeinschaft under contract HO1125/20-1,2.

References

[1] Flory F, Escoubas L and Berginc G 2011 *J. Nanophoton.* **5** 052502
[2] Banholzer M J, Millstone J E, Qin L D and Mirkin C A 2008 *Chem. Soc. Rev.* **37** 885
[3] Ko H, Singamaneni S and Tsukruk V V 2008 *Small* **4** 1576
[4] Singh A V, Vyas V, Patil R, Sharma V, Scopelliti P E, Bongiorno G, Podesta A, Lenardi C, Gade W N and Milani P 2011 *PLoS One* **6** e25029

[5] Kriparamanan R, Aswath P, Zhou A, Tang L and Nguyen K T 2006 *J. Nanosci. Nanotechnol.* **6** 1905

[6] Toma A, Chiappe D, Boragno C and Buatier de Mongeot F 2010 *Phys. Rev.* B **81** 165436

[7] Oates T W H, Keller A, Facsko S and Mücklich A 2007 *Plasmonics* **2** 47

[8] Fazio B *et al* 2011 *ACS Nano* **5** 5945

[9] Zhang K, Uhrmacher M, Hofsass H and Krauser J 2008 *J. Appl. Phys.* **103** 083507

[10] Zhang K, Rotter F, Uhrmacher M, Ronning C, Krauser J and Hofsass H 2007 *New J. Phys.* **9** 29

[11] Sato K, Okamoto I, Kitamoto Y and Ishida S 2007 *Japan. J. Appl. Phys.* 1 **46** 5139

[12] Büttner F, Zhang K, Seyffarth S, Liese T, Krebs H U, Vaz C A F and Hofsäss H 2011 *Phys. Rev.* B **84** 064427

[13] Zhan Q-F, Vandezande S, Van Haesendonck C and Temst K 2007 *Appl. Phys. Lett.* **91** 122510

[14] Liedke M O, Liedke B, Keller A, Hillebrands B, Mücklich A, Facsko S and Fassbender J 2007 *Phys. Rev.* B **75** 220407

[15] Smirnov V K, Kibalov D S, Orlov O M and Graboshnikov V V 2003 *Nanotechnology* **14** 709

[16] Ozaydin G, Özkan A S, Wang Y, Ludwig K F, Zhou H, Headrick R L and Siddons D P 2005 *Appl. Phys. Lett.* **87** 163104

[17] Ozaydin-Ince G and Ludwig K F Jr 2009 *J. Phys.: Condens. Matter* **21** 224008

[18] Sánchéz-García J A, Vázquez L, Gago R, Redondo-Cubero A, Albella J M and Czigány Zs 2008 *Nanotechnology* **19** 355306

[19] Macko S, Frost F, Ziberi B, Förster D and Michely T 2010 *Nanotechnology* **21** 085301

[20] Zhang K, Brötzmann M and Hofsäss H 2011 *New J. Phys.* **13** 013033

[21] Macko S, Frost F, Engler M, Hirsch D, Höche T, Grenzer J and Michely T 2011 *New J. Phys.* **13** 073017

[22] Cornejo M, Ziberi B, Meinecke C, Hirsch D, Gerlach J W, Höche Th, Frost F and Rauschenbach B 2011 *Appl. Phys.* A **102** 593

[23] Hofsäss H, Zhang K, Pape A, Bobes O and Brötzmann M 2013 *Appl. Phys.* A **111** 653

[24] Hofsäss H and Zhang K 2009 *Nucl. Instrum. Methods* B **267** 2731

[25] Hofsäss H, Zhang K and Zutz H 2009 *Nucl. Instrum. Methods* B **267** 1398

[26] Hofsäss H and Zhang K 2008 *Appl. Phys.* A **92** 517

[27] Hofsäss H, Brötzmann M and Zhang K 2012 *AIP Adv.* **2** 032123

[28] Redondo-Cubero A, Gago R, Palomares F J, Mücklich A, Vinnichenko M and Vázquez L 2012 *Phys. Rev.* B **86** 085436

[29] Macko S, Grenzer J, Frost F, Engler M, Hirsch D, Fritzsche M, Mücklich A and Michely Th 2012 *New J. Phys.* **14** 073003

[30] Zhang K, Hofsäss H and Zutz H 2010 *Nucl. Instrum. Methods* B **268** 1967

[31] Zhou J, Facsko S, Lu M and Möller W 2011 *J. Appl. Phys.* **109** 104315

[32] Hofsäss H, Zhang K, Gehrke H G and Brötzmann M 2013 *Phys. Rev.* B **88** 075426

[33] Bradley R M 2013 *Phys. Rev.* B **87** 205408

[34] Uhrmacher M and Hofsäss H 2005 *Nucl. Instrum. Methods* B **240** 48

[35] www.gwyddion.net

[36] Lauterborn W and Kurz T 2003 *Coherent Optics—Fundamentals and Applications* 2nd edn (Berlin: Springer)

[37] Sanchéz-García J A, Gago R, Caillard R, Redondo-Cubero A, Martin-Gago J A, Palomares F J, Fernández M and Vázquez L 2009 *J. Phys.: Condens. Matter* **21** 224009

[38] Ziberi B, Cornejo M, Frost F and Rauschenbach B 2009 *J. Phys.: Condens. Matter* **21** 224003

[39] Ziberi B, Frost F and Rauschenbach B 2006 *J. Vac. Sci. Technol.* A **24** 1344

[40] Ziegler J, Biersack J P and Ziegler M D 2008 *SRIM—The Stopping and Ranges of Ions in Solids* (Chester: SRIM Co.) www.srim.org